



Contents lists available at ScienceDirect

Journal of Alloys and Compounds

journal homepage: <http://www.elsevier.com/locate/jalcom>

A green and template recyclable approach to prepare Fe₃O₄/porous carbon from petroleum asphalt for lithium-ion batteries



Yang Liu^a, Peng Li^a, Yuwei Wang^b, Jingyan Liu^a, Yang Wang^a, Jinqiang Zhang^a,
Mingbo Wu^{a,*}, Jieshan Qiu^{b,**}

^a State Key Laboratory of Heavy Oil Processing, China University of Petroleum, Qingdao 266580, China

^b Carbon Research Laboratory, State Key Lab of Fine Chemicals, School of Chemical Engineering, Dalian University of Technology, Dalian 116024, China

ARTICLE INFO

Article history:

Received 4 August 2016

Received in revised form

3 November 2016

Accepted 11 November 2016

Available online 12 November 2016

Keywords:

Magnetite

Petroleum asphalt

Mesoporous carbon

Recyclable template

Lithium-ion battery

ABSTRACT

In this work, a green and template-recyclable method was designed to obtain Fe₃O₄/petroleum asphalt based carbons (Fe₃O₄/PC) with different Fe₃O₄ contents as anode material for Li-ion batteries. 73-Fe₃O₄/PC with 73% Fe₃O₄ can deliver a high reversible capacity of 785 mAh g⁻¹ at 200 mA g⁻¹ with excellent stability. The superior electrochemical performance of as-made Fe₃O₄/PC is attributed to the good electrical conductivity of carbon framework from asphalt and its dimensional confinement on Fe₃O₄ nanoparticles. This study not only demonstrates a green and economical route for high-value utilization of petroleum asphalt in energy storage, but also paves a new way for the preparation of porous carbon via recyclable template, which is indispensable for green chemistry.

© 2016 Elsevier B.V. All rights reserved.

1. Introduction

Transition-metal oxides as anode materials of Li-ion batteries (LIBs) have attracted much attention due to their larger specific capacities compared with 372 mAh g⁻¹ of graphite [1–7]. Unfortunately, serious volume change commonly occurs during cycling processes and low conductivity dramatically hinder the stability of LIBs with metal oxide as electrode material. In order to avoid above shortcomings, many efforts have been intensively carried on metal oxide electrode. Carbon coating [8,9], Fe₃O₄@carbon hybrid [10–12], and Fe₃O₄/graphene composites [13,14] have been systematically prepared as excellent alternative electrodes, showing superior electrochemical capacity and durability in comparison to Fe₃O₄ electrode. However, the yields of carbon are extremely low and the preparation is difficult to scale up owing to the limitations of the complicated fabrication methods and the expensive raw materials in some of previous works [10,11]. Thus, it is imperative to develop a simple and effective way for mass production of metal oxide/carbon materials from cheap carbon sources.

As the heaviest by-product of petroleum distillation [15], petroleum asphalt has not been fully utilized in the down-stream petrochemical processes due to its complex structure. However, the asphalt with high carbon content and plentiful polycyclic aromatic hydrocarbons has been directly converted to graphene and nanoporous carbon frameworks, e.g. graphene foam [16,17], carbon fibers [18,19] and porous carbon materials [20,21], which have good application future in the fields of water purification, gas adsorption, energy storage and conversion, etc. Luckily, many efforts have been made in the design of coal-based nanocarbon materials [22,23], which give us good reference to construct nanocarbon materials from petroleum asphalt.

The preparation of carbon materials from petroleum asphalt has already been intensively reported. Xu et al. synthesized graphene framework from asphalt with the assistance of vermiculite absorbent, which showed excellent electrochemical properties in LIBs [24]. Hollow carbon capsules facilitating the stability of overall electrochemical behavior for cathode of Li-S battery have been prepared from petroleum pitch via template approach [20]. Methods for synthesizing asphalt-derived carbon materials can be grouped roughly into two types: one is the carbon materials prepared by carbonization and dehydrogenation of asphalt [25–27], such as carbon fibers via melt-spinning process, nanoporous carbon by sacrificing template, which are very complicated, letting

* Corresponding author.

** Corresponding author.

E-mail addresses: wumb@upc.edu.cn (M. Wu), jqiu@dlut.edu.cn (J. Qiu).

alone the low yields and the hard-controlled qualities. Besides, nano-template and acid solution cannot be recycled. Another is based on the decomposition of carbon sources and the growth of nanocarbon materials via catalytic gas or vapor deposition [28,29], typically including the preparation of nanotube or fullerene through macromolecule decomposing and self-assembly of small carbon molecules. This strategy is also tedious and requires an especially precise control of experimental parameters.

Taken these problems into account, we developed a green and economic template recycling method to prepare Fe_3O_4 /asphalt based porous carbon (Fe_3O_4 /PC) with tailored mesoporous structure as anode material for LIBs. Fe_2O_3 nanoparticles act as template and Fe precursor reused in the later electrode material preparation. After the subsequent template recycling process, Fe_3O_4 nanoparticles were evenly distributed on PC, which is conducive to the accommodation of continuous expansion/shrinkage and the efficient utilization of more active sites. Thus, as-fabricated nanocomposites possess superior electrochemical performance. This economic methodology is in line with the green chemistry and paves a new way for high-value utilization of heavy oil.

2. Experimental

2.1. Preparation of PC

Petroleum asphalt from China National Offshore Oil Corp. (17.63 wt% of saturates, 31.13 wt% of aromatics, 38.21 wt% of resins and 6.40 wt% of asphaltenes) was used as carbon precursor. Other chemicals were purchased from Aladdin, and used as received.

In a typical run, 2.5 g asphalt was wholly dissolved in 20 mL toluene with the assistance of ultrasonication. A brown solution was obtained and then heated to 110 °C in oil bath. Meanwhile, 10 g nano- Fe_2O_3 template (ca. 30 nm in diameter) was gradually added under continuous stirring, and evaporated for 8 h. After cooling to room temperature, the resultant mixture was collected and transferred into a tube furnace. After keeping for 1 h in N_2 atmosphere, it was then heated at 800 °C for 1 h. After cooling down to room temperature, the sample was washed with 2 M HCl solution and distilled water thoroughly to remove the iron template and dried at 80 °C, then PC was finally obtained. The acid washed template liquid (AWTL) was collected and recycled for the preparation of Fe_3O_4 /PC.

2.2. Preparation of Fe_3O_4 /PC composites

To obtain Fe_3O_4 /PC with evenly distributed Fe_3O_4 , the addition of Fe species in AWTL to as-made PC is needed, and the reason is given in Fig. 1 in Supporting Information. To synthesize 73% Fe_3O_4 /

PC (73- Fe_3O_4 /PC, as an example), 0.3 g PC was dispersed in 150 mL alcohol-water (1:2, v/v) solution by sonication (denoted as A) and a certain amount of AWTL was adjusted to 100 mL by distilled water (denoted as B). Then solution A and B were mixed by agitation and the pH was adjusted to 9–10 by adding diluted ammonia solution dropwise. The obtained composite was filtered and dried at 60 °C, followed by calcination at 400 °C in air for 2 h to obtain Fe_3O_4 /PC composite. Fe_3O_4 /PC composites with different Fe_3O_4 contents were prepared by adjusting the amount of AWTL. Fe_3O_4 contents were tested by thermogravimetric analysis.

2.3. Sample characterization

As-made samples were characterized by X-ray diffraction (XRD) (X'Pert PRO MPD, Holland) using Cu K α radiation ($\lambda = 1.518$ Å). The pore structure was investigated by low temperature nitrogen adsorption-desorption isotherms on a sorptometer (Micromeritics, ASAP 2020, USA). Transmission electron microscopy (TEM) (JEM-2100UHR, Japan) and field emission scanning electron microscopy (FE-SEM, S4800, Japan) were used to investigate the structure and morphology of as-obtained samples. X-ray photoelectron spectroscopy analyses were conducted on a Kratos Axis Ultra instrument (Chestnut Ridge, NY). The crystallinity of as-made samples was labeled by Raman analysis carried out by a Jobin-Yvon Labram-010 Raman spectrometer. Thermogravimetric analysis (TGA) (STA 409 PC Luxx, Germany) was carried out under air flow of 200 mL min⁻¹ with a temperature ramp of 10 °C min⁻¹.

2.4. Electrochemical measurements

The working electrodes were prepared by coating homogeneous slurry consisting of as-made Fe_3O_4 /PC, polyvinylidene difluoride (PVDF) binder and carbon black with a weight mass of 80:10:10 dissolved in *N*-methyl-2-pyrrolidinone on a copper foil. After dried at 100 °C for 10 h, the electrode was roll-pressed and assembled into a half-battery in an argon-filled glove box in which the concentrations of water and oxygen were controlled below 0.1 ppm. CR2032 half-cell were assembled from bottom to top by packing working electrode, separator and counter electrode, i.e. Fe_3O_4 /PC, microporous polypropylene film and Li foil, with 1 mol L⁻¹ LiPF₆ in a 1:1 (v/v) mixture of ethylene carbonate and dimethyl carbonate as the electrolyte. After sealed and aged for 12 h, the cells were galvanostatically charged-discharged in the potential range of 0.01–3 V vs. Li/Li⁺ at the current density of 200 mA g⁻¹ on a battery testing system (Land CT2001A). Cyclic voltammetry (CV) curves were tested at 0.2 mV s⁻¹ in the range of 0.01–3 V by Ametek PARSTAT4000 electrochemistry workstation. Electrochemical impedance spectroscopy (EIS) tests were also tested by Ametek

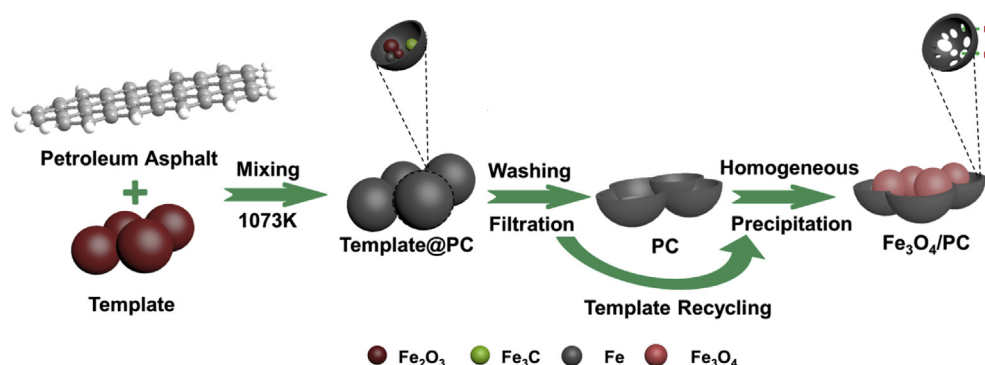


Fig. 1. Schematic of Fe_3O_4 /PC nanohybrids via recyclable template strategy.

PARSTAT4000 electrochemistry workstation in the frequency range of 100 kHz to 10 mHz with AC voltage amplitude 10 mV.

3. Results and discussion

$\text{Fe}_3\text{O}_4/\text{PC}$ hybrids were obtained by template recycling method as illustrated in Fig. 1. Nano- Fe_2O_3 and asphalt dissolved in toluene were mixed under energetic agitation at a weight ratio of 4:1 to get a homogeneous mixture. During the subsequent heat treatment at 800 °C under N_2 atmosphere, Fe_2O_3 acts as template as well as activation agent, both of which are conducive to the formation of plentiful mesopores in the carbonization process [23]. Developed porous structure in PC can benefit the homogeneous precipitation of $\text{Fe}(\text{OH})_3$ and $\text{Fe}(\text{OH})_2$ during the subsequent recycling of AWTL via coprecipitation of Fe-containing species, which are eventually transformed into Fe_3O_4 NPs with a small particle size of 20–50 nm during the calcination in air. The huge specific surface area of PC makes it easy to trap Fe_3O_4 NPs and they can interact tightly via Van der Waals forces [30,31]. Notably, the simplicity and economization of the template recycling route is favorable for the scalable preparation and industrial application of $\text{Fe}_3\text{O}_4/\text{PC}$.

As the active material for lithium ion storage, Fe_3O_4 NPs play an important role on the electrochemical performance of $\text{Fe}_3\text{O}_4/\text{PC}$ electrode. In Fig. S2, the accurate weight percentages of Fe_3O_4 in $\text{Fe}_3\text{O}_4/\text{PC}$ hybrids were evaluated by TGA, which are close to the loading amounts in advance (35, 50, 75, 85 wt%), validating the practicability of template recycling method employed in the preparation of $\text{Fe}_3\text{O}_4/\text{PC}$ for LIBs.

Fig. 2(a) shows the XRD patterns of template@PC and pure PC after template removal. Besides Fe_2O_3 , other Fe-containing species can also be identified, including Fe (JCPDS no. 06-0696) and Fe_3C (JCPDS no. 65-2411), which may be attributed to chemical redox reaction between Fe_2O_3 and amorphous carbon. The diffraction peaks of acid washed PC at 25° and 43° correspond to the (002) and (001) planes of graphite, respectively [24,25], and the calculated $d(002)$ and $d(001)$ are larger than those of graphite. The XRD patterns of $\text{Fe}_3\text{O}_4/\text{PC}$ nanohybrids with different Fe_3O_4 loading contents are illustrated in Fig. 2(b), in which all peaks can be attributed to the cubic magnetite (JCPDS no.65-3107), indicating the completed transformation to crystalline Fe_3O_4 at 400 °C in air. As the Fe_3O_4 content increases, the peaks of the crystalline Fe_3O_4 become stronger. The XRD data reveals that the synthesized products are mainly composed of Fe_3O_4 and PC after recyclable AWTL loading, without any other Fe phase.

The porosity of the ultrathin carbon layers covering on the surface of template can be identified in the TEM image of Template@PC in Fig. 3(a). The morphologies of Fe_2O_3 template are irregular, and even aggregate, which might facilitate the formation

of uneven structure and massive pores in PC as shown in Fig. 3(b). Fig. 3(c) and (d) are the low and high magnification TEM images of PC washed by HCl solution and deionized water, transparently illustrating the honeycomb-like structure with innumerable pores. PC NPs with different size pores and walls consisting of several graphene layers can be clearly observed by high resolution TEM shown in Fig. 3(d). After the subsequent template recycling process, Fe_3O_4 NPs can be widely dispersed into PC, and their sizes are relatively narrower (in range of 5–20 nm) in comparison to template@PC in Fig. 3(a). By contrast, the pure Fe_3O_4 NPs shown in Fig. S3(a) are highly aggregated and in non-uniform. Fe_3O_4 NPs occupy more porous sites of PC matrix with their increasing incorporated content. For 37- $\text{Fe}_3\text{O}_4/\text{PC}$ in Fig. 3(b), there are not enough Fe_3O_4 NPs to fully cover the surface of PC, resulting in a relatively small size of the fabricated Fe_3O_4 NPs (around 20 nm). As the content of incorporated Fe_3O_4 goes up to 53 wt% (Fig. S3(c)), some macropores are inhabited by the incorporated Fe_3O_4 NPs that tend to aggregate to form relatively large Fe_3O_4 nanocrystals (in range of 20–30 nm). As for Fe_3O_4 NPs of 73- $\text{Fe}_3\text{O}_4/\text{PC}$, there is no obvious change in size and the PC is uniformly decorated (Fig. 3(e)). However, conspicuous aggregation occurs in 81- $\text{Fe}_3\text{O}_4/\text{PC}$ (Fig. S3(d)). Thus, 73 wt% is appropriate for Fe_3O_4 particles to disperse on PC. In Fig. 3(f), a lattice spacing of 0.25 nm in accord with the (311) plane of Fe_3O_4 can be clearly identified. The SAED pattern in the inset of Fig. 3(f) exhibits a polycrystallinity nature and the diffraction rings can be readily indexed to the crystal planes of the inverse spinel Fe_3O_4 phase, which is consistent with the XRD result [34] and further demonstrates the feasibility of this template recycling approach.

As shown in Fig. S4, Raman spectroscopy was used to further investigate the microstructure of PC and 73- $\text{Fe}_3\text{O}_4/\text{PC}$. G band around 1585 cm^{-1} corresponds to the first order scattering of the E_{2g} mode of sp^2 carbon domains, while D band (near 1340 cm^{-1}) is related to the disordered microstructure [9–11]. The intensity ratio (I_D/I_G) of 73- $\text{Fe}_3\text{O}_4/\text{PC}$ is 1.02, larger than 0.92 of PC, indicating that the degree of disorder increases as a result of the incorporation of Fe_3O_4 . The Brunauer–Emmett–Teller (BET) specific surface area and porous structure of 73- $\text{Fe}_3\text{O}_4/\text{PC}$ and pure PC have been characterized by nitrogen adsorption–desorption isotherms (Fig. S5). Compared to PC prepared via ZnO template [26], PC in this work has a bigger specific surface area, i.e. $724\text{ m}^2\text{ g}^{-1}$ under the same preparation condition, which mainly attributes to the in-situ activation induced by Fe_2O_3 , and this can also be proved by the reduced Fe and Fe_3C in Fig. 2(a). In other words, Fe_2O_3 plays two roles in the preparation of PC, i.e. template and active agent, the reaction between Fe_2O_3 and amorphous carbon can make new pores, which can facilitate the subsequent template recycling process. The mesoporous structure of 73- $\text{Fe}_3\text{O}_4/\text{PC}$ deduced from Fig. S5(b) not

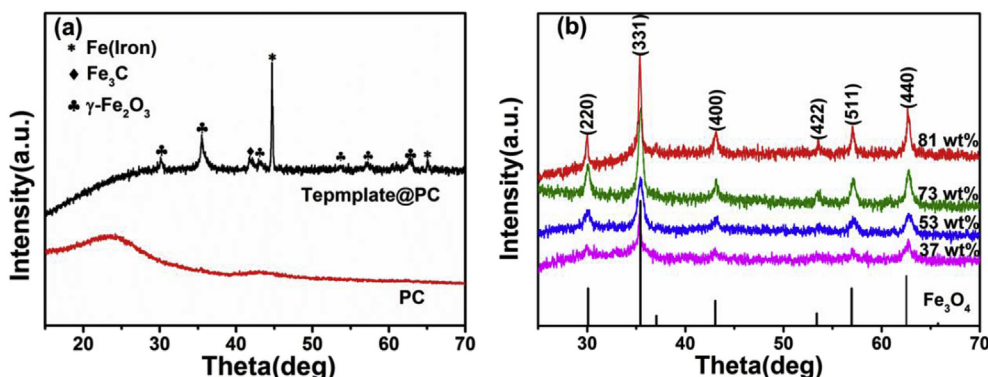


Fig. 2. X-ray diffraction (XRD) patterns of (a) Template@PC and pure PC, (b) $\text{Fe}_3\text{O}_4/\text{PC}$ nanohybrids with different Fe_3O_4 contents.

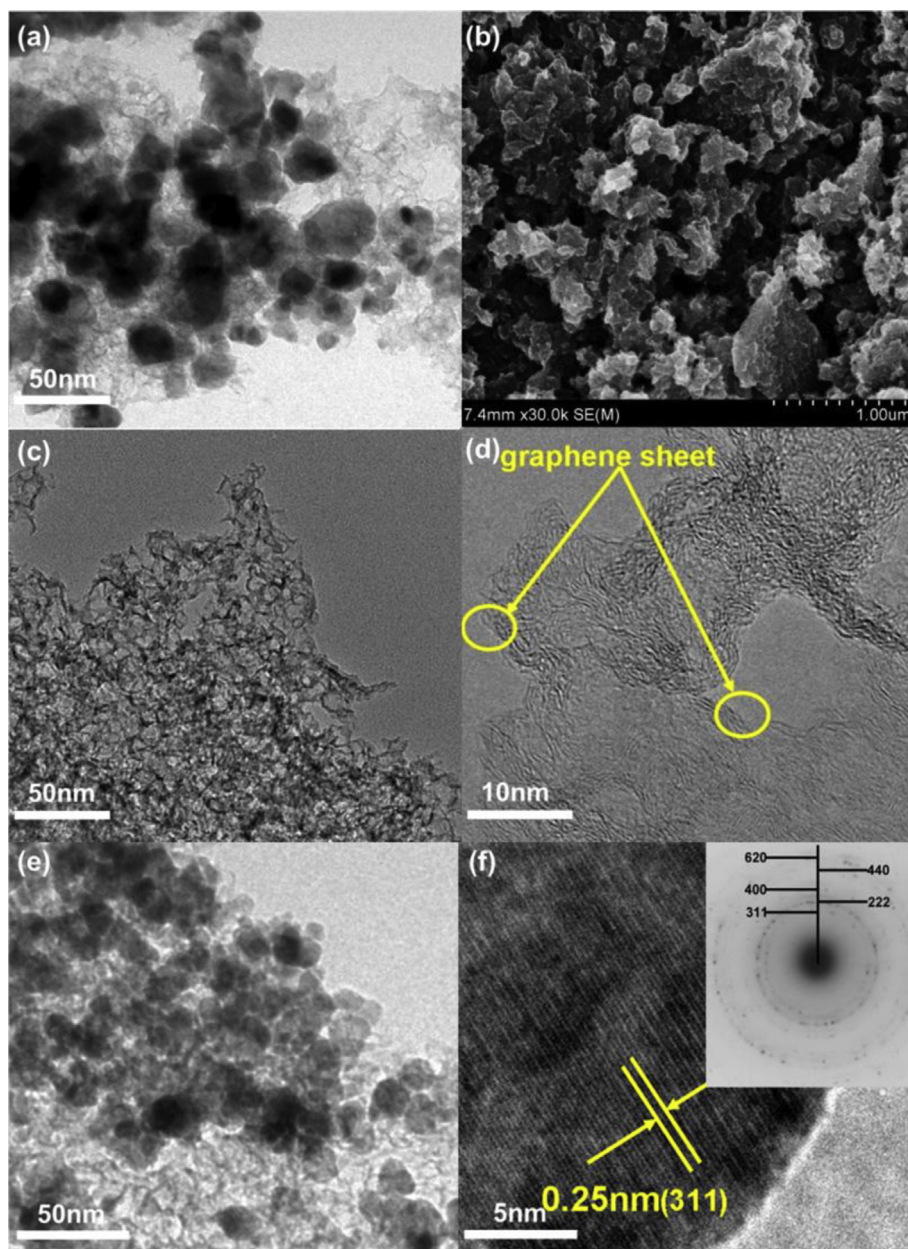


Fig. 3. TEM image of Template@PC (a), FESEM image of pure PC (b), Low and high magnification TEM images of pure PC (c, d) and 73-Fe₃O₄/PC nanohybrid (e, f). (inset in f) Selected area electron diffraction (SAED) pattern for 73-Fe₃O₄/PC.

only favors the confinement of Fe₃O₄ but also allows the easy access and transport of charge and electron in charge-discharge processes. 73-Fe₃O₄/PC exhibits a typical type IV isotherm with a H₁ hysteresis loop, similar with that of pure PC sample. Due to the filling of Fe₃O₄ NPs into the massive pores, the average pore size and the pore volume of 73-Fe₃O₄/PC are 14 nm and 0.88 cm³ g⁻¹ respectively, much lower than 20 nm and 2.94 cm³ g⁻¹ of pure PC [30].

X-ray photoelectron spectroscopy measurement (XPS) has also been utilized to investigate the chemical composition of Fe₃O₄/PC. The spectrum in Fig. 4(a) indicates the presence of carbon, oxygen, iron and negligible nitrogen in 73-Fe₃O₄/PC. For the Fe 2p spectrum (Fig. 4(b)), two peaks at 711 eV and 725 eV correspond to the Fe 2p_{3/2} and Fe 2p_{1/2} peaks of Fe₃O₄, respectively. The spin-orbit split Fe 2p peaks are broad due to a small chemical shift difference between Fe²⁺ and Fe³⁺ present in Fe₃O₄. Moreover, the absence of an obvious satellite peak situated at ~719 eV, which is the fingerprint

of the electronic structure of Fe₃O₄, also confirms that Fe₃O₄ rather than Fe₂O₃ is present. This is an important way to distinguish between Fe₃O₄ (magnetite) and γ-Fe₂O₃ (maghemite) since they have the same crystal structure but different valence states of iron ions [29,31]. For the O1s spectrum (Fig. 4(c)), the low binding energy peak centered at 530.3 eV corresponds to the O²⁻ bonded with iron (lattice oxygen in Fe₃O₄), and the high energy peak at 533.4 eV can be assigned to C–O and O–C=O bonds [32–34]. A small shoulder around 531.8 eV between the two dominating peaks should originate from surficial –OH groups. The high resolution C1s spectrum in Fig. 4(d) exhibits three peaks at 284.8, 286.6 and 289 eV, in accord with sp² bonded carbon (C–C) in carbon network, carbonyls (C=O), and carboxyls (O–C=O).

The electrochemical performance of 73-Fe₃O₄/PC electrode was investigated using cyclic voltammetry (CV) performed at a scanning rate of 0.1 mV s⁻¹ (Fig. 5). In the first discharge process, two

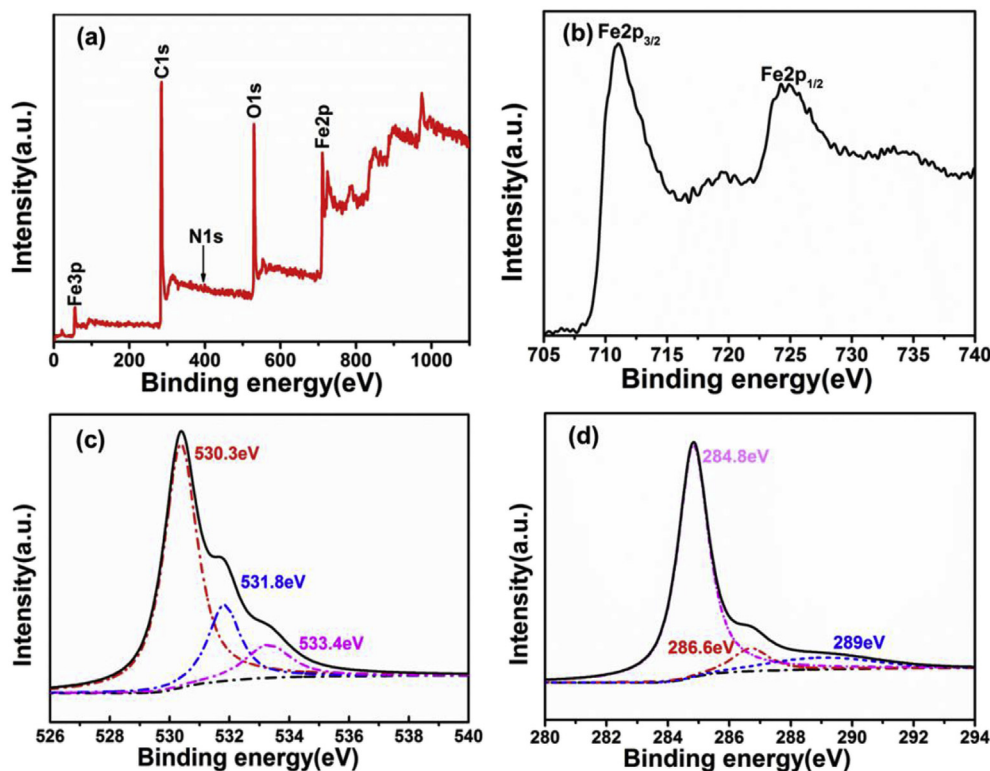
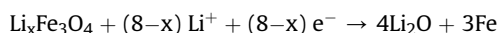
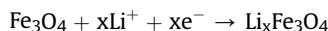


Fig. 4. XPS spectrum of 73-Fe₃O₄/PC nanohybrid, and high resolution XPS spectrum of (b) Fe 2p, (c) O 1s, (d) C 1s from 73-Fe₃O₄/PC.

well-defined reduction peaks around 0.73 and 0.92 V represent the gradual reduction of Fe³⁺ and Fe²⁺ to Fe⁰ combined with the formation of solid electrolyte interface (SEI) layer [34–36], as shown in the following conversion reactions:



Meanwhile, the multiple anodic peaks between 1.6 and 1.9 V in the subsequent cycles are attributed to the oxidation of Fe⁰ to Fe²⁺ and Fe³⁺. After the second cycle, the CV curves of the Fe₃O₄/PC electrode are well overlapped, indicating good electrochemical reversibility. Furthermore, if 8 Li⁺ can be removed reversibly, the

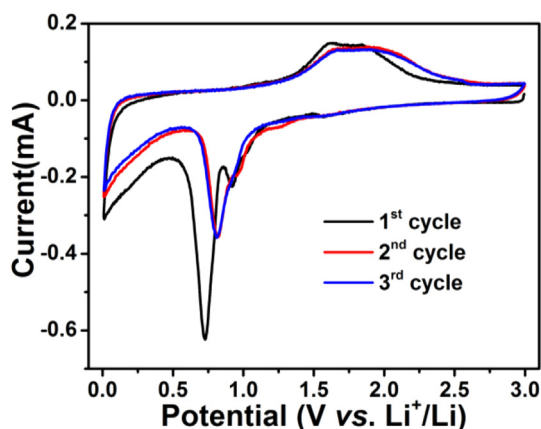


Fig. 5. Cyclic voltammograms for 73-Fe₃O₄/PC electrode at a scan rate of 0.1 mV s⁻¹ with a voltage window from 3 to 0.01 V.

theoretic capacity (922 mAh g⁻¹) of Fe₃O₄ in the anodic process can be calculated from above equations [14,36].

The charge–discharge curves of 73-Fe₃O₄/PC electrode at a current density of 200 mA g⁻¹ are given in Fig. 6(a). The initial discharge capacity of 73-Fe₃O₄/PC electrode is 1375 mAh g⁻¹, obviously outperforming the theoretic capacity of Fe₃O₄ electrode, which could be attributed to the synergistic effects between PC and Fe₃O₄ in the anodic process [9–13]. And the first charge capacity is 860 mAh g⁻¹, resulting in a coulombic efficiency of 63% due to the adverse effect derived from high specific surface area mentioned above [4,5]. The first discharge curve at ~0.8 V can be attributed to the SEI layers formed on the PC surface [34], and after the first cycle, the coulombic efficiencies of 73-Fe₃O₄/PC can keep above 99% in the following cycles. The specific capacities of the 5th, 10th and 100th cycles remain nearly unchanged, suggesting a good cycle stability of 73-Fe₃O₄/PC. Fig. 6(b) demonstrates the cycling performance of 73-Fe₃O₄/PC at 200 mA g⁻¹, which exhibits stable cycling performance and maintains a specific capacity of about 785 mAh g⁻¹ after 100 cycles, showing better lithium storage ability and cycling stability than those of reported Fe₃O₄/carbon anode in literature, e.g. graphene-wrapped Fe₃O₄ (800 mAh g⁻¹, 175 mA g⁻¹) [14], graphene-Fe₃O₄ (637 mAh g⁻¹, 200 mA g⁻¹) [13], carbon coated Fe₃O₄ (749 mAh g⁻¹, 200 mA g⁻¹) [34]. The outstanding electrochemical performance of 73-Fe₃O₄/PC could be attributed to the synergistic effect of appropriate loading amount of Fe₃O₄, PC matrices with porous structure, size and position confinements of PC on Fe₃O₄. In order to make sure the roles of PC and Fe₃O₄ in Fe₃O₄/PC electrode, pure Fe₃O₄ NPs and Fe₃O₄/PC with various Fe₃O₄ contents at same current density are given in Fig. 6(c). Obviously, PCs from petroleum asphalt with loaded Fe₃O₄ have preferable electrochemical performance and PCs can act as electron conductor during the electrochemical process. In particular, 81-Fe₃O₄/PC, 53-Fe₃O₄/PC and 37-Fe₃O₄/PC show only 250, 700 and 680 mAh g⁻¹, respectively at a current density of

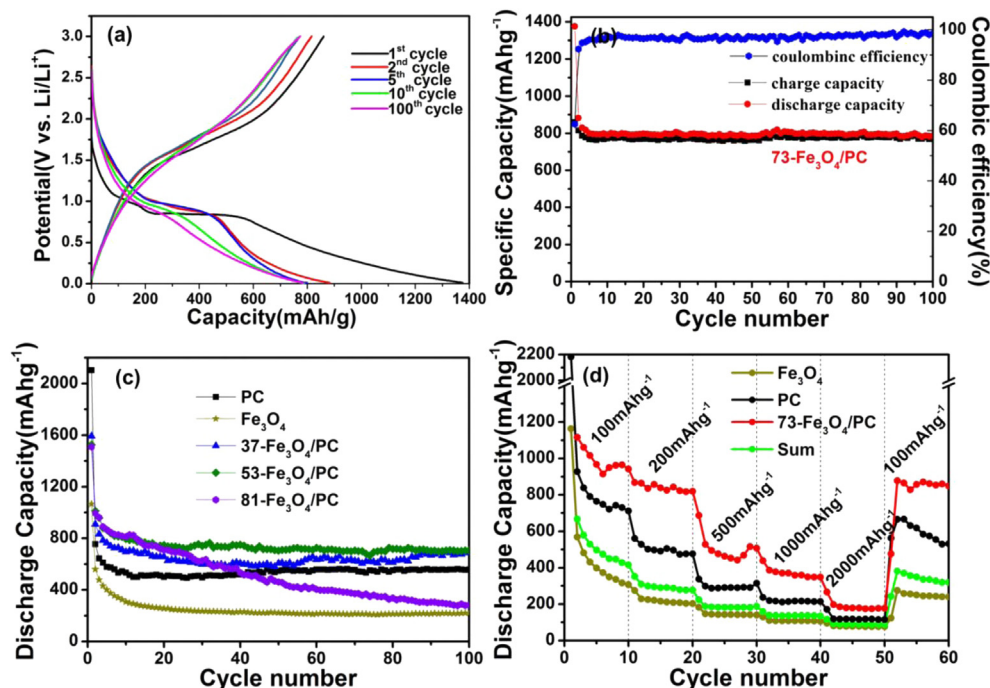


Fig. 6. (a) Lithium insertion/extraction properties of 73-Fe₃O₄/PC electrode. (b) The coulombic efficiency and the cycling performance of 73-Fe₃O₄/PC at a current density of 200 mA g⁻¹. (c) The discharge capacity of pure PC, Fe₃O₄, 81-Fe₃O₄/PC, 53-Fe₃O₄/PC and 37-Fe₃O₄/PC at a current density of 200 mA g⁻¹. (d) The discharge performance of Fe₃O₄, PC and 73-Fe₃O₄/PC at various current rates. The line of “Sum” represents the sum of capacities of Fe₃O₄ and PC accounting for their percentages in 73-Fe₃O₄/PC (according to the equation: Sum capacity = 0.73 × capacity_{Fe₃O₄} + 0.27 × capacity_{PC}).

200 mA g⁻¹. Thus, 73 wt% is the most suitable weight ratio of Fe₃O₄ for the electrochemical properties of Fe₃O₄/PC electrode.

Fig. 6(d) shows the rate performance of PC, pure Fe₃O₄ and 73-Fe₃O₄/PC electrodes at different current densities. The specific capacity of 73-Fe₃O₄/PC is always much higher than those of PC and pure Fe₃O₄. At a current density of 1 A g⁻¹, the discharge capacity of 73-Fe₃O₄/PC is 350 mAh g⁻¹, which is much higher than 170 mAh g⁻¹ of PC and 78 mAh g⁻¹ of pure Fe₃O₄. Moreover, 73-Fe₃O₄/PC shows superior specific capacities at different current densities compared with the “Sum” capacities, which again verifies the critical role of synergistic effect between Fe₃O₄ and PC in composite. Cycling performance of 73-Fe₃O₄/PC at current density of 800 mA g⁻¹ is shown in Fig. S6. A reversible capacity of 500 mAh g⁻¹ can still be remained after 300 cycles, showing an extraordinary cycling stability of 73-Fe₃O₄/PC even at 800 mA g⁻¹.

To gain further insight into the relationship between electrochemical performance and electrode kinetics after the introduction of PC via recyclable template technique, EIS are performed on Fe₃O₄/PC and bare Fe₃O₄ electrodes, as shown in Fig. 7. The Nyquist plots are similar to each other in shape, exhibiting a typical Randles-model behavior [34,35], which consists of a semicircle in the high-to-middle frequency domain and a linear Warburg tail in the low frequency region. The intercept on the Z' axis at the high-frequency area is the electrolyte resistance (R_s) and the size of the semicircular is related to the charge-transfer resistance (R_{ct}), and the inclined line in the low-frequency region represents the Warburg impedance (Z_w) related to lithium diffusion in the solid. Apparently, the impedances of Fe₃O₄/PC electrode (~50 Ω) are much smaller than 100 Ω of pure Fe₃O₄ electrode, indicating that PC incorporation can dramatically promote the electrochemical properties of Fe₃O₄/PC, which is consistent with the results from charge–discharge curves. The enhanced electrochemical performances of Fe₃O₄/PC could be ascribed to the developed porous channels of PC providing fast diffusion channels for Li⁺ [37,38].

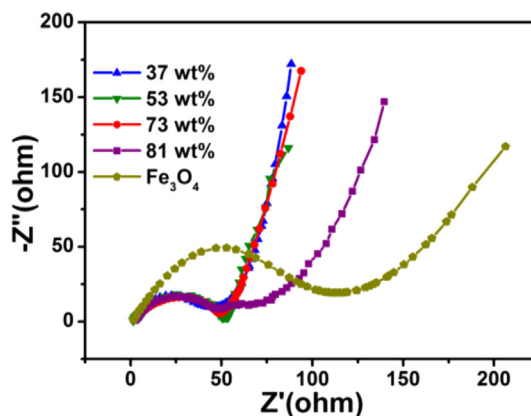


Fig. 7. Nyquist plots of pure Fe₃O₄ and four Fe₃O₄/PC composites with different contents of Fe₃O₄ at a discharge potential of 0.1 V (vs. Li/Li⁺) from 100 kHz to 0.01 Hz.

Meanwhile, the high conductivity of carbon skeleton derived from petroleum asphalt guarantees the fast charge/discharge processes.

4. Conclusion

Fe₃O₄/PC nanohybrids with different Fe₃O₄ contents were successfully prepared from petroleum asphalt via a green and template recycling approach. Multifunctional Fe₂O₃ acts as template and activation agent for pore formation, and providing Fe species for Fe₃O₄/PC electrode. As LIBs anode material, 73-Fe₃O₄/PC can deliver a high reversible capacity of 785 mAh g⁻¹ at 200 mA g⁻¹ even after 100 cycles, much higher than those of PC and bare Fe₃O₄. The improved capacities and excellent cycling stability are ascribed to the porous carbon framework confining Fe₃O₄ nanoparticles and shortening the distance of Li⁺ transportation as well as synergistic

effects existed between PC and Fe_3O_4 . This work paves a new way in recycling the nanotemplate and improving the high-value utilization of asphalt. Furthermore, this green approach can also be extended to build other metal oxide/porous carbon nanocomposites for catalysis, gas sensing, etc.

Acknowledgements

This work was supported by the National Natural Science Foundation of China (Nos. 51372028, 21302224, 51372277); the Fundamental Research Fund for the Central Universities (No. 15CX08005A).

Appendix A. Supplementary data

Supplementary data related to this article can be found at <http://dx.doi.org/10.1016/j.jallcom.2016.11.168>.

References

- [1] P. Poizat, S. Laruelle, S. Grugeon, L. Dupont, J.-M. Tarascon, *Nature* 407 (2000) 496–499.
- [2] C.M. Park, J. Kim, H. Kim, H. Kim, *Chem. Soc. Rev.* 39 (2010) 3115–3141.
- [3] X.H. Li, Y.B. He, C. Miao, X.Y. Qin, W. Lv, H.D. Du, B.H. Li, Q.H. Yang, F. Kang, *Carbon* 81 (2015) 739–747.
- [4] P. Li, J.Y. Liu, Y. Liu, Y.W. Wang, Z.T. Li, W.T. Wu, Y. Wang, L.H. Yin, H. Xie, M.B. Wu, X.J. He, J.S. Qiu, *Electrochim. Acta* (2015) 164–172.
- [5] G.L. Wu, Z.T. Li, W.T. Wu, M.B. Wu, *J. Alloys Compd.* 615 (2014) 582–587.
- [6] Y.S. Hu, R.D. Cakan, M. Titirici, J. Mller, M. Antonietti, *Angew. Chem. Int. Ed.* 47 (2008) 1645–1649.
- [7] F. Han, D. Li, W.C. Li, C. Lei, Q. Sun, A.H. Lu, *Adv. Funct. Mater.* 23 (2013) 1692–1700.
- [8] J.E. Lee, S. Yu, D.J. Lee, D. Lee, S.I. Han, Y. Sung, T. Hyeon, *Energy Environ. Sci.* 5 (2012) 9528–9533.
- [9] Y. Chen, B.H. Song, M. Li, L. Lu, J.M. Xue, *Adv. Funct. Mater.* 24 (2014) 319–326.
- [10] Y.C. Dong, K. Md, Y.S. Chui, Y. Xia, C. Cao, J. Lee, J.A. Zapien, *Electrochim. Acta* 176 (2015) 1332–1337.
- [11] T. Yoon, C. Chae, Y. Sun, X. Zhao, H.H. Kung, J.K. Lee, *J. Mater. Chem.* 21 (2011) 17325–17330.
- [12] Y.Z. Wan, Z.W. Yang, G.Y. Xiong, H.L. Luo, *J. Mater. Chem. A* 3 (2015) 15386–15393.
- [13] J. Su, M.H. Cao, L. Ren, C.W. Hu, *J. Phys. Chem. C* 115 (2011) 14469–14477.
- [14] G.M. Zhou, D.W. Wang, F. Li, L.L. Zhang, N. Li, Z.S. Wu, L. Wen, G.Q. (Max) Lu, H.M. Cheng, *Chem. Mater.* 22 (2010) 5306–5313.
- [15] J. Murgich, J.M. Rodriguez, Y. Aray, *Energy Fuels* 10 (1996) 68–76.
- [16] M.X. Wang, C.Y. Wang, T.A. Li, M.M. Cheng, Z.J. Hu, *New Carbon Mater.* 24 (2009) 61–66.
- [17] S. Park, Y. Jang, J. Shim, S. Ryu, *J. Colloid Interface Sci.* 260 (2003) 259–264.
- [18] M.X. Wang, C.Y. Wang, T.Q. Li, Z.J. Hu, *Carbon* 46 (2008) 84–91.
- [19] F. Derbyshire, R. Andrews, D. Jacques, M. Jagtoyen, G. Kimber, T. Rantell, *Feul* 80 (2001) 345–356.
- [20] N. Jayaprakash, J. Shen, Surya S. Moganty, A. Corona, Lynden A. Archer, *Angew. Chem.* 723 (2011) 6026–6030.
- [21] L.Q. Wang, J.Z. Wang, F. Jia, C.Y. Wang, M.M. Chen, *J. Mater. Chem. A* 1 (2013) 9498–9507.
- [22] X.J. He, H.B. Zhang, H. Zhang, X.J. Li, N. Xiao, J.S. Qiu, *J. Mater. Chem. A* 2 (2014) 19633–19640.
- [23] X.J. He, N. Zhao, J.S. Qiu, N. Xiao, M.X. Yu, C. Yu, X.Y. Zhang, M.D. Zheng, *J. Mater. Chem. A* 1 (2013) 9440–9448.
- [24] C.G. Xu, G.Q. Ning, X. Zhu, G. Wang, X.F. Liu, J.S. Gao, Q. Zhang, W.Z. Qian, F. Wei, *Carbon* 62 (2013) 213–221.
- [25] Z.C. Liu, Z.Q. Tu, Y.F. Li, F. Yang, S. Han, W. Yang, L.Q. Zhang, G. Wang, C.M. Xu, J.S. Gao, *Mater. Lett.* 122 (2014) 285–288.
- [26] P. Li, J.Y. Liu, Y.W. Wang, Y. Liu, X.N. Wang, K. Nam, Y. Kang, M.B. Wu, J.S. Qiu, *Chem. Eng. J.* 286 (2016) 632–639.
- [27] J.S. Qiu, Y.L. An, Z.B. Zhao, Y.F. Li, Y. Zhou, *Fuel Process. Technol.* 85 (2004) 913–920.
- [28] J.S. Qiu, Q.X. Li, Z.Y. Wang, Y.F. Sun, H.Z. Zhang, *Carbon* 44 (2006) 2565–2568.
- [29] L.W. Yin, Z.W. Zhang, Z.Q. Li, F.B. Hao, Q. Li, C.X. Wang, R.H. Fan, Y.X. Qi, *Adv. Funct. Mater.* 24 (2014) 4176–4185.
- [30] M. Du, C. Xu, J. Sun, L. Gao, *J. Mater. Chem. A* 1 (2013) 7154–7158.
- [31] F. Han, L.J. Ma, Q. Sun, C. Lei, A.H. Lu, *Nano Res.* 7 (2014) 1706–1717.
- [32] T. Yamashita, P. Hayes, *Appl. Surf. Sci.* 9 (2007) 4322–4329.
- [33] C.N. He, S. Wu, N.Q. Zhao, C.S. Shi, E.Z. Liu, J.J. Li, *Acs Nano* 7 (2013) 4459–4469.
- [34] J.S. Luo, J.L. Liu, Z.Y. Zeng, C.F. Ng, L.J. Ma, H. Zhang, J.Y. Lin, Z.X. Shen, H.J. Fan, *Nano Lett.* 13 (2013) 3136–3143.
- [35] W.M. Zhang, X.L. Wu, J.S. Hu, Y.G. Guo, L.J. Wan, *Adv. Funct. Mater.* 18 (2008) 3941–3946.
- [36] T. Yamada, K. Morita, K. Kume, H. Yoshikawa, K. Awaga, *J. Mater. Chem. C* 2 (2014) 5183–5188.
- [37] Z.M. Cui, L.Y. Jiang, W.G. Song, Y.G. Guo, *Chem. Mater.* 21 (2009) 1162–1166.
- [38] T. Zhu, J.S. Chen, X.W. (David) Lou, *J. Phys. Chem. C* 115 (2011) 9814–9820.